

LA-UR-16-26121

Approved for public release; distribution is unlimited.

Title:	The resistive wall instability in multi-pulse linear induction accelerators
Author(s):	Ekdahl, Carl August Jr.
Intended for:	21st International Conference on High Power Particle Beams, 2016-09-18/2016-09-22 (Estoril, Portugal)
Issued:	2017-03-13 (rev.1)

Disclaimer:

Los Alamos National Laboratory, an affirmative action/equal opportunity employer, is operated by the Los Alamos National Security, LLC for the National Nuclear Security Administration of the U.S. Department of Energy under contract DE-AC52-06NA25396. By approving this article, the publisher recognizes that the U.S. Government retains nonexclusive, royalty-free license to publish or reproduce the published form of this contribution, or to allow others to do so, for U.S. Government purposes. Los Alamos National Laboratory requests that the publisher identify this article as work performed under the auspices of the U.S. Department of Energy. Los Alamos National Laboratory strongly supports academic freedom and a researcher's right to publish; as an institution, however, the Laboratory does not endorse the viewpoint of a publication or guarantee its technical correctness.

The Resistive-Wall Instability in Multi-Pulse Linear Induction Accelerators

Carl Ekdahl, *Fellow, IEEE*

Abstract—The resistive wall instability results from the Lorentz force on the beam due to the beam image charge and current. If the beam pipe is perfectly conducting, the electric force due to the image charge attracts the beam to the pipe wall, and, the magnetic force due to the image current repels the beam from the wall. For a relativistic beam, these forces almost cancel, leaving a slight attractive force, which is easily overcome by external magnetic focusing. However, if the beam pipe is not perfectly conducting, the magnetic field due to the image current decays on a magnetic-diffusion time scale. If the beam pulse is longer than the magnetic diffusion time the repulsion of the beam tail will be weaker than the repulsion of the beam head. In the absence of an external focusing force, this causes a head-to-tail sweep of the beam toward the wall. This instability is usually thought to be a concern only for long-pulse relativistic electron beams. However, with the advent of multi-pulse, high-current linear induction accelerators (LIAs) the possibility of pulse-to-pulse coupling of this instability should be investigated. We have explored pulse-to-pulse coupling using the LAMDA beam dynamics code, and we present results of this investigation.

Index Terms—Intense relativistic electron beams, Electron beam instabilities, Linear induction accelerators

I. INTRODUCTION

THE resistive wall instability is usually thought to be a concern only for long-pulse relativistic electron beams [1, 2, 3, 4]. However, with the advent of multi-pulse, high-current linear induction accelerators (LIAs) [5, 6, 7, 8, 9] the possibility of pulse-to-pulse coupling of this instability should be investigated. In earlier papers [10, 11] estimates of instability growth in drift transport regions of multi-pulse machines were based on analytic theory. A quantitative examination of the pulse-to-pulse coupling phenomenon using direct simulation of the forces on the beam is the thrust of this article.

The instability results from the Lorentz force on the beam due to the beam images charge and current in the conducting beam pipe. If the pipe is perfectly conducting, the electric force due to the image charge attracts the beam to the pipe wall. However, the magnetic force due to the image current repels the beam from the wall. For a relativistic beam, these

forces almost cancel, leaving an attractive force equal to $1/\gamma^2$ times the image charge force, where γ is the Lorentz relativistic mass factor. However, if the beam pipe is not perfectly conducting, the magnetic field due to the image current decays on a time scale $\tau_d \propto \sigma$, where σ is the pipe conductivity. Thus, if the beam pulse length τ_p is greater than τ_d the magnetic repulsion of the beam tail will be weaker than the repulsion of the beam head. In the absence of an external focusing force, this causes a head-to-tail sweep of the beam toward the wall. This sweep grows as the beam propagates down the pipe. The strong external focusing force provided by the solenoidal magnetic fields of an LIA complicate this simple picture, but generally do provide significant suppression of instability growth.

For a constant-current coasting beam the time-varying electromagnetic fields produced by the conducting-wall images of a beam displaced a distance $\xi(t)$ from the centerline were derived in [2]. These fields are proportional to $\xi(t)$, and for early times, the resulting radial force on the beam toward the wall is approximately

$$\mathbf{F}(z, t) = \mathbf{e}_x \left[\frac{2eI}{b^2 \beta c \gamma^2} \xi(z, t) + \frac{4eI\beta}{\gamma \pi b^3 \sqrt{\sigma}} \int_{-\infty}^t \frac{d\xi}{dt'} \sqrt{t-t'} dt' \right] \quad (1)$$

where e is the electron charge, I is the beam current, b is the beam pipe radius, $\beta\gamma = \sqrt{\gamma^2 - 1}$ is the normalized electron momentum [3]. Except where noted, cgs units are used in this article. The first term is the force that would be applied for a perfectly conducting wall, and the integral term represents the decay of the magnetic repulsion due to diffusion of the dipole field. Adding a uniform axial magnetic field, B , results in the equation of motion given in [3];

$$\frac{d^2 \xi}{dt^2} + (k_\beta \beta c)^2 \xi = \frac{e}{m} \left[\frac{2I}{b^2 \beta c \gamma^2} \xi(z, t) + \frac{4I\beta}{\gamma \pi b^3 \sqrt{\sigma}} \int_{-\infty}^t \frac{d\xi}{dt'} \sqrt{t-t'} dt' \right] \quad (2)$$

where m is the electron mass, and the betatron wavenumber is $k_\beta = eB / 2mc\beta\gamma = B_{KG} / 3.4\beta\gamma \text{ cm}^{-1}$.

Submitted for review on May ??, 2016. This work was supported by the National Nuclear Security Administration of the U. S. Department of Energy under contract number DE-AC52-06NA25396.

The author is with the Los Alamos National Laboratory, Los Alamos, NM 87545 USA (e-mail: cekdahl@lanl.gov).

Eq. (2) is immediately recognized as a *wakefield equation*. That is, the transverse force on every beam electron is due to the conducting tube wall images of the preceding electrons, but not of those following it (due to relativistic causality) [12]. Thus, the transverse force on the last electron in the pulse is due to the images of all of the rest of the electrons preceding it in the pulse. It follows that an electron in a second pulse following the first is also subject to a transverse forces due to images of all of the electrons preceding it, including those in the first pulse. This is pulse-to-pulse coupling. The reductio ad absurdum is; if there is no gap between the two pulses, this case is indistinguishable from a single pulse of greater length than the first.

The analytic theory of [3] does not account for time varying currents, and so cannot explore pulse-to-pulse coupling. Nor does it account for accelerated beams in non-uniform magnetic focusing fields, as occur in a real accelerator. Therefore, we use the beam dynamics code LAMDA (Linear Accelerator Model for DARHT) [13] for this investigation.

II. SIMULATIONS

To simulate the motion of a beam, LAMDA subdivides it into many disks of length $\Delta\tau$ and applies the fundamental equation of motion

$$\frac{d\mathbf{p}}{dt} = -e \left[\mathbf{E} + \frac{\mathbf{v}}{c} \times \mathbf{B} \right] \quad (3)$$

to each disk. Cartesian coordinates are used for the centroid motion calculations. The electromagnetic fields include those due to external focusing and wall images, as well as higher order corrections for beam diamagnetism and curvature of its trajectory [14]. The resistive wall instability algorithm breaks the beam pipe up into segments much shorter than the beam disks, resolves the force given by Eq. (1) into its Cartesian components, and applies an impulse to each beam disk equal to the force multiplied by the time for the disk to traverse the short pipe segment [13].

Moreover, the developers of LAMDA accommodated time varying currents by recognizing that, as derived in [2], the image fields are proportional to $\xi(t)I(t)$ without loss of generality. Thus, as implemented in LAMDA, the integrand in Eq. (1) is proportional to $\partial\xi I / \partial t$, rather than $\partial\xi / \partial t$. This feature enables calculations for time varying currents, and in particular, multiple beam pulses.

A. Region of Applicability

As previously noted, the image electromagnetic fields giving rise to the force equation (1) are an approximation, which is only valid for early times. Thus, the LAMDA simulations are only applicable for times $t \ll \tau_1 = 4\sigma\Delta^2 / c^2$ and $t \ll \tau_d$ [2], where τ_d is the dipole field decay time $\tau_d = 2\pi\sigma b\Delta / c^2$ in a thin-walled non-magnetic beam pipe of inner radius b and thickness Δ [15]. Since beam pipes usually have wall thickness Δ less than b , the second of

these relations is automatically satisfied if the first is. For example, a stainless steel ($\sigma = 1.15 \times 10^{16} \text{ s}^{-1}$) pipe with 15-cm ID and 0.32-cm wall has $\tau_1 \approx 5 \mu\text{s}$. This pipe size is rather typical for short-pulse LIAs, and is used for many of the simulations in this article. In this pipe, LAMDA predictions for short pulses $< 100 \text{ ns}$ are well within the limitations of the theory, but only marginally so for pulses as long as 2-3 μs .

B. Single Pulse

We first use LAMDA to illustrate the nature of the instability by considering a 10-MeV, 2-kA, 1- μs pulse coasting through a 7.5-cm radius stainless-steel beam pipe in a uniform 500-G magnetic guide field. A key result of the analytic theory is that the characteristic distance for significant growth is

$$z_g(\tau) = \frac{4\gamma}{I_{kA}\sqrt{\tau_{\mu s}}} \left(\frac{\sigma_{s^{-1}}}{10^{17}} \right)^{1/2} \left(\frac{b_{cm}}{10} \right)^3 \left(\frac{100}{2\pi} k_{0m^{-1}} \right) \text{ m} \quad (4)$$

where τ is time into the pulse measured back from the head, and the units for the parameters are indicated by the subscripts [3]. Here, the space-charge reduced betatron wavelength k_0 is defined by

$$k_0^2 = k_\beta^2 - \frac{2I_{kA}}{17(\beta\gamma)^3} \frac{1}{b^2} \quad (5)$$

Worth noting is the strong dependence of the characteristic distance on the size of the beam pipe; $z_g \propto b^3$, which favors large beam pipes for long-pulse machines. LAMDA simulations follow this scaling law (see Appendix A).

For our illustrative beam pulse, $z_g = 70 \text{ m}$, so we choose that distance as the beam pipe length in order to observe the growth of the instability. The entire beam pulse is attracted toward the wall by the images, but the beam tail more so than the beam head, because of the weakening magnetic image. The 500-G guide field is enough to suppress the motion of the beam head. To show this, in Fig. 1 we compare the instability amplitude at the beam tail ($\tau = 1000 \text{ ns}$) as a function of distance with the amplitude at 50 ns into the pulse (which would also be the tail amplitude for a 50-ns pulse).

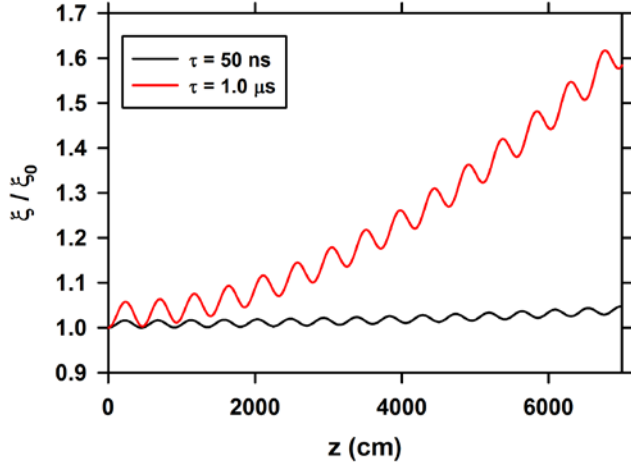


Fig. 1. LAMDA simulation of single-pulse resistive wall instability amplitude for a 2-kA, 10-MeV coasting beam in a 500-G uniform guide field. (red) Tail of 1.0 μ s pulse (black) 50-ns into pulse.

Since the experimenter will be interested in how this instability might appear in data, we also show the trajectory of the beam centroid during the pulse as it might appear in data from a beam position monitor (BPM) at the end of the 70-m pipe [16]. In Fig. 2 it is seen that the manifestation of this instability is a slow head-to-tail radial drift toward the wall impressed on the cycloidal $\mathbf{F} \times \mathbf{B}$ drift. The azimuthal location of the beginning of drift locus is simply the phase advance, $k_0 z$.

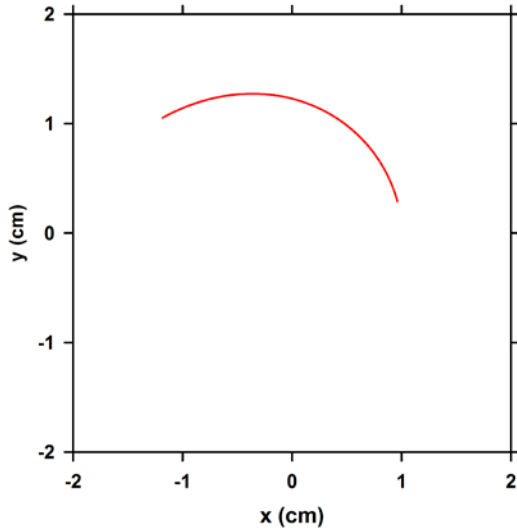


Fig. 2. LAMDA simulation of beam transverse motion at the end of the 70-m pipe as it might appear in BPM data for a beam with an initial 1-cm offset in x .

An important property of this instability in a strong magnetic guide field is that the head-to-tail growth of the instability is nearly independent of beam energy. According to Eq. (5), k_0 is almost inversely proportional to γ , especially for high energy. It follows from Eq. (4) that z_g is almost

independent of γ . The significance of this is that results for a coasting beam can be generalized to an accelerated beam. Moreover, this property is useful for experimentally distinguishing between corkscrew motion [17, 18], which can be strongly correlated with beam energy variations, and resistive wall instability, which is not [16, 19].

This energy independence is clearly seen in LAMDA simulations. Fig. 3 shows the displacement of the tail of the pulse as a function of distance, as in Fig. 1. The three curves plotted are for 5-MeV, 10-MeV, and 15-MeV. The displacement at the end of the pipe is nearly independent of beam energy. In Fig. 4, we compare the centroid trajectories as might be measured with a BPM at the end of the pipe. Other than the phase shift, there is little to distinguish these trajectories, again showing insensitivity to beam energy.

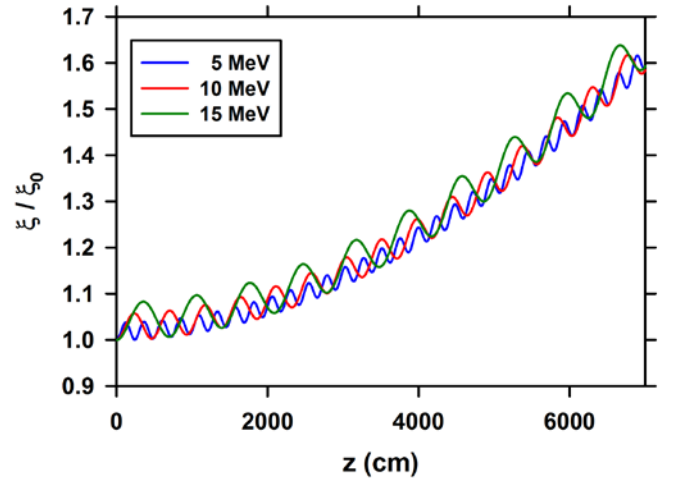


Fig. 3. LAMDA simulation of resistive wall instability amplitude for a 2-kA coasting beam in a 500-G uniform guide field. (blue) 5-MeV beam energy (red) 10-MeV beam energy (green) 15-MeV beam energy

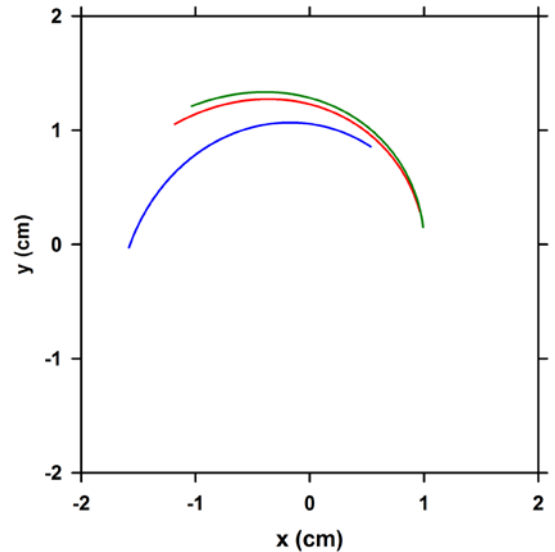


Fig. 4. LAMDA simulation of beam transverse motion at the end of the 70-m pipe for different beam energies. (blue) 5-

MeV beam energy (red) 10-MeV beam energy (green) 15-MeV beam energy.

C. Multiple Pulse

In order to demonstrate the coupling of the resistive wall instability in multiple pulses we first consider two 2-kA, 10-MeV pulses with a 100-ns flattop and 10-ns rise and fall times. The beam pipe is the same as used for single-pulse simulations, but the transport magnetic field has been reduced to 200 G to enhance the growth in order to clearly demonstrate the effect.

First, consider the two pulses as close together as possible (Fig. 5). This is almost the same as a single pulse with twice the length. Next consider the second pulse substantially delayed as shown in Fig. 6.

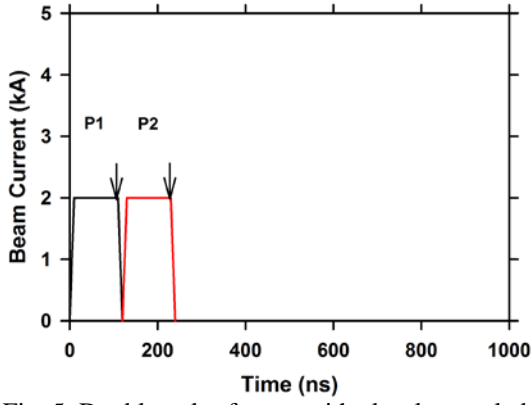


Fig. 5. Double pulse format with closely coupled pulses. The arrows mark the times for which amplitude is plotted in Fig. 7.

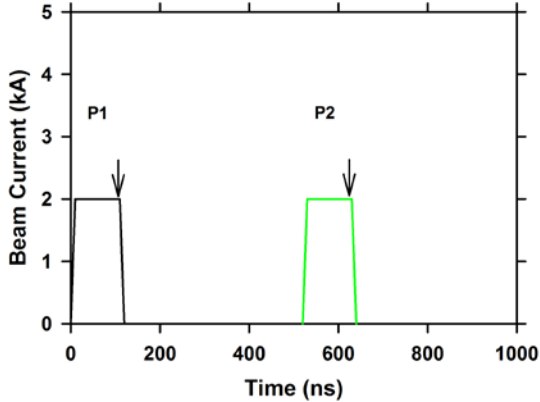


Fig. 6. Double pulse format with widely separated pulses. The arrows mark the times for which amplitude is plotted in Fig. 7.

In Fig. 7 we compare the amplitude as a function of distance for the first pulse at the end of its flattop ($\tau_1 = 110$ ns) with the amplitude of the second pulse at the end of its flattop ($\tau_2 = 110$ ns). The extra growth at the tail of the second pulse is due to the image fields of the first pulse, which are strongest when the second pulse begins immediately after the first pulse ends (delay = 0 ns). As the second pulse is further delayed, the

field due to the first pulse weakens, and the extra growth is less. These simulations clearly show the pulse-to-pulse coupling of the instability.

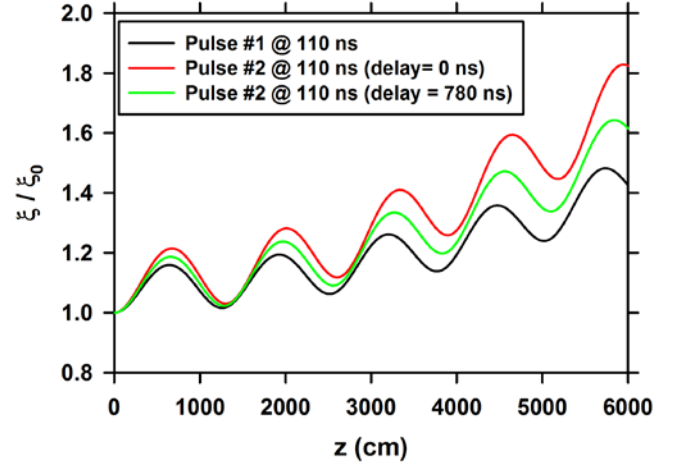


Fig. 7. LAMDA simulation of instability amplitude on two pulses. Amplitude was calculated at times shown by markers in Fig. 5 and Fig. 6. (black) Amplitude at end of first pulse. (red) Amplitude at end of second pulse with pulses closely coupled as shown in Fig. 5. (green) Amplitude at end of second pulse with pulses widely separated as shown in Fig. 6.

Finally, we study the coupling effect as it might manifest in a real multi-pulse LIA. For example, consider a hypothetical accelerator with a 2-kA, 2-MeV multi-pulse injector that accelerates the beam to 20-MeV through 72 cells. The 250-kV cells are grouped in blocks of 4 cells each, with vacuum pumping in between. Using solenoidal magnetic focusing optimized to suppress beam-breakup while minimizing corkscrew motion would result in the field shown in Fig 8, where the field strength varies as $\sqrt{\gamma}$ [20], and the initial field is strong enough to stabilize the image displacement instability [21, 22, 20].

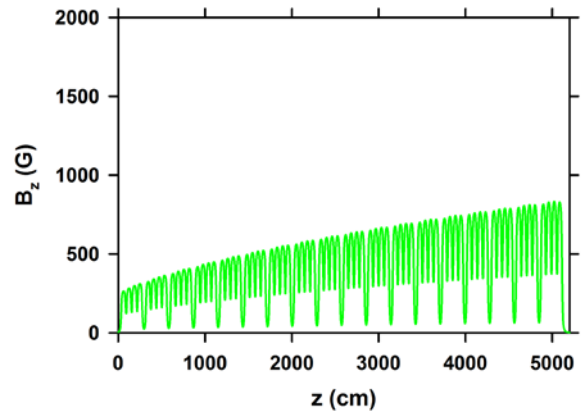


Fig. 8. Solenoidal magnetic field on axis needed to suppress beam breakup in a 2-kA, 20-MeV LIA. The increase in field strength with distance is optimized to minimize corkscrew motion according to [20].

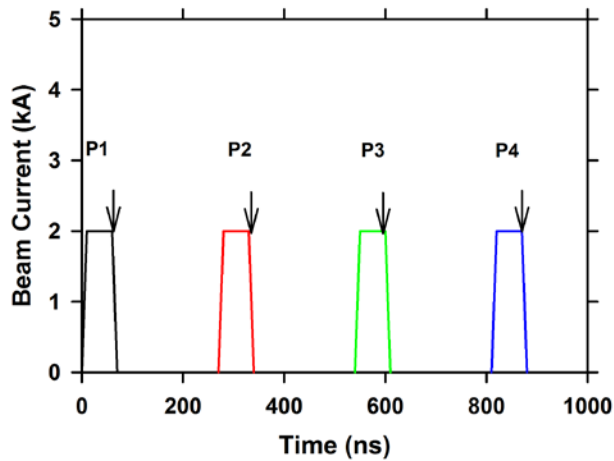


Fig.9. Four-pulse format of the injected electron beam. Arrows indicate the times for which the instability amplitude was calculated.

Now, consider the 4-pulse format shown in Fig. 9 for the injected beam. Each pulse has a 50-ns flat-top, and 10-ns rise and fall. They are separated by 200 ns. This pulse train is less than $1\mu\text{s}$ in duration, so barely within the constraints of the theory. Fig. 10 shows LAMDA calculations of the resistive wall instability amplitude at the times shown by the markers in Fig. 9. Although there is slight evidence of coupling, the magnetic focusing field of Fig. 8 is strong enough that the instability is damped and the beam focused toward the axis. Thus, pulse-to-pulse coupling is not expected to be a problem in any real multi-pulse LIA having similar parameters.

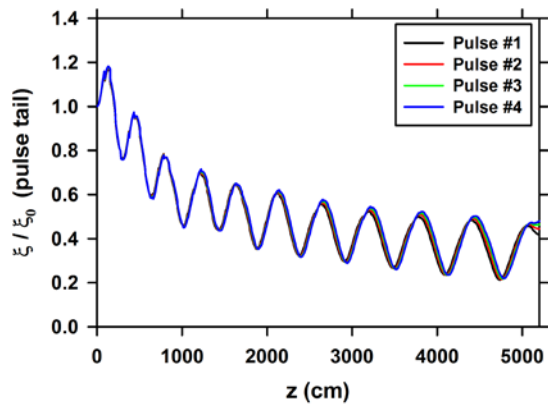


Fig. 10. LAMDA simulation of the instability attenuation due to the strong magnetic focusing shown in Fig. 8. (black) Tail of pulse #1. (red) Tail of pulse #2. (green) Tail of pulse #3. (blue) Tail of pulse #4.

On the other hand, the situation can be quite different in the downstream transport of the beam from the accelerator to the experimental area. This beamline might be quite long, with few focusing magnets and long drifts where there is no

magnetic field to suppress the instability. For example, Fig. 11 shows the magnetic focusing in the downstream transport beamline of the short-pulse LIA in operation at the Los Alamos National Laboratory [23, 24, 25]. If the four 2-kA, 20-MeV pulses were to be transported through this beamline the instability amplitude would grow as shown in Fig. 12. Here, the pulse-to-pulse coupling is very evident, and it would cause a spread in the positions of the focal spots, as well as a smear of the spot sizes.

Fortunately, this problem can be mitigated by using a downstream beam pipe made of higher conductivity material, such as aluminum or copper alloy. Fig. 13 shows the calculated amplitude and coupling resulting from the use of aluminum alloy pipe ($\sigma = 2.0 \times 10^{17} \text{ s}^{-1}$) instead of stainless steel. By comparing Fig. 12 and Fig. 13, it is evident that a significant reduction of spread between the amplitude of pulse #1 and amplitude of pulse #4 results from this substitution of materials. An additional benefit of using higher conductivity materials is that it substantially enlarges the regime of applicability of the theory. For example, switching from stainless steel to aluminum alloy changes τ_1 from $\tau_1 = 5 \mu\text{s}$ to $\tau_1 = 87 \mu\text{s}$, so LAMDA predictions for pulse trains as long as 2 or 3 μs would be well within the constraints of the theory.

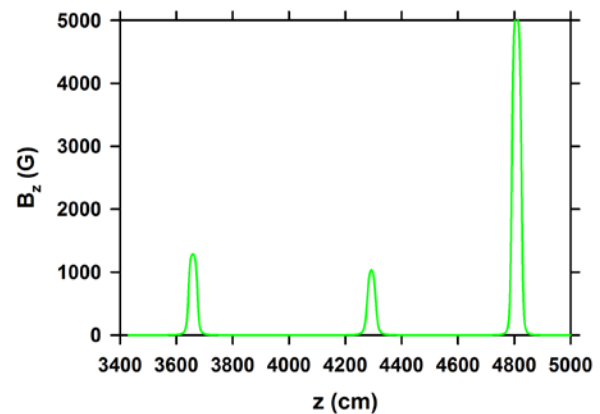


Fig. 11. Solenoidal magnetic focusing fields in the downstream transport beamline of the short-pulse LIA at Los Alamos National Laboratory.

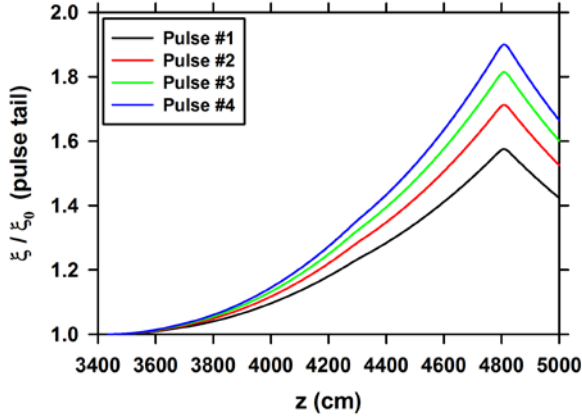


Fig. 12. LAMDA simulated instability growth on the tails of the four pulses shown in Fig. 9. Beam transported through the downstream beamline shown in Fig. 11 with stainless steel beam pipe. Amplitude was calculated at the times marked in Fig. 9. (black) Tail of pulse #1. (red) Tail of pulse #2. (green) Tail of pulse #3. (blue) Tail of pulse #4.

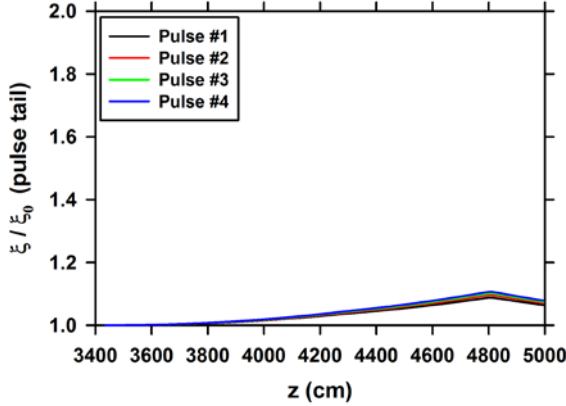


Fig. 13. LAMDA simulated instability amplitude on the tails of the four pulses shown in Fig. 9. Beam transported through the downstream beamline shown in Fig. 11, but using aluminum alloy beam pipe. Amplitude was calculated at the times marked in Fig. 9. (black) Tail of pulse #1. (red) Tail of pulse #2. (green) Tail of pulse #3. (blue) Tail of pulse #4.

Of course, another option for mitigation is to use a larger beam pipe. To obtain the same reduction in growth as switching to aluminum would only require increasing the beam pipe size by $\sim 60\%$ (to $b = 12$ cm). This is very close to the standard vacuum tubing size having $b = 12.3$ cm, so switching to this size should provide as much suppression as does the use of aluminum.

III. CONCLUSIONS

Computer simulations with the LAMDA beam dynamics code have demonstrated pulse-to-pulse coupling of the resistive wall instability. The magnetic guide fields in high-

current LIAs are generally strong enough to suppress this effect.

Pulse-to-pulse coupling can be especially troublesome in the downstream transport of the beam from the accelerator to an experimental area. These transport beamlines generally have long drifts with no magnetic field, so the growth of the instability, and of coupling, can be significant. If it is expected to be a problem with stainless steel pipe, then it can be mitigated through the use of more highly conducting beam pipes made from aluminum or copper alloys. This substitution also extends the regime of applicability by more than an order of magnitude. Alternatively, increasing the size of the beam pipe is an especially effective mitigation measure, because the characteristic distance for significant growth is proportional to the cube of the pipe size.

What is missing from this discussion is experimental validation of the theory, and we are exploring opportunities to do just that.

APPENDIX A

The growth of the resistive hose instability as simulated by LAMDA is nearly exponential with distance. In this Appendix we use LAMDA simulations to deduce the e-folding lengths quantifying this exponential growth. The e-folding length is a function of the parameters of the physical situation; beam current and pulse width, electron energy, pipe size and conductivity, and magnetic guide field. To determine how the e-folding length scales with these parameters, we are guided by the characteristic lengths dimensionally deduced in [3]. Since the parametric scaling of those analytic characteristic lengths are dimensionally correct, showing that LAMDA e-folding lengths have the same scaling provides some validation of the physical reality of the simulations.

Characteristic lengths for instability growth were given in [3] for the case of continuous magnetic focusing, and also for the case of just enough magnetic focusing to exactly cancel the beam space-charge defocusing, i.e., $k_0 = 0$. We use the parametric scaling of these analytic lengths in what follows.

A. No Magnetic Guide Field

Although no analytic scaling law is given in [3] for the situation where there is no magnetic guiding field ($k_\beta = 0$), the authors did use dimensional analysis to estimate a characteristic growth length for $k_0 = 0$, in which case there are no terms proportional to ξ in Eq. (2). As derived by the authors of [3], this characteristic length is

$$\ell_g \approx \frac{3.8\gamma^{1/2}}{I_{kA}^{1/2}\tau_{\mu s}^{1/4}} \left(\frac{\sigma_{s^{-1}}}{10^{17}} \right)^{1/4} \left(\frac{b_{cm}}{10} \right)^{3/2} \text{ m} \quad (6)$$

As verified with LAMDA simulations, the $k_0 = 0$ parametric scaling of growth length also holds for the zero field case, at least in the parameter range of interest for linear induction accelerators explored here.

As shown in Fig. A1, with no magnetic field the instability grows nearly exponentially, $\xi / \xi_0 \approx \exp(z / \zeta_0)$. The e-folding length ζ_0 is a function of the parameters of the problem, such as beam current, energy, and pulsewidth; as well as beam-pipe size and material. To verify that the $k_0 = 0$ parametric scaling also holds for the zero field case ($k_\beta = 0$), we varied the parameters in the range shown in Table I (with $B = 0$), and plotted the amplitude ξ / ξ_0 at 20 m as a function of the variable

$$p_0 = \frac{I_{kA}^{1/2} \tau_{\mu s}^{1/4}}{\gamma^{1/2} b_{cm}^{3/2} (10^{-16} \sigma_{s^{-1}})} \quad m^{-1} \quad (7)$$

Thus, if the characteristic length scaling given by Eq. (6) is valid for these simulations, a semi-log plot should follow a straight line, as it does, as shown in Fig. A2. From the slope of a least squares fit to these data one gets the e-folding length ζ_0

$$\zeta_0 = 0.0799 \frac{\gamma^{1/2} b_{cm}^{3/2} (\sigma_{s^{-1}} / 10^{16})^{1/4}}{I_{kA}^{1/2} \tau_{\mu s}^{1/4}} \quad m \quad (8)$$

Comparing Eq. (8) with Eq. (6) shows that the e-folding length ζ_0 is about 20% greater than the characteristic length ℓ_g derived in [3]. Thus, past use of ℓ_g as a predictor of resistive wall problems [26] has been a conservative approach.

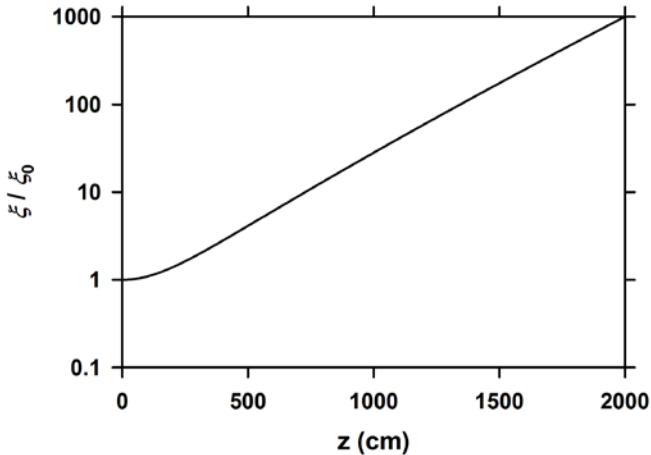


Fig. A1: LAMDA simulation of growth of the tail of a 1-ms, 2-kA, 10-MeV beam pulse in a 5-cm radius stainless steel tube with no magnetic guide field.

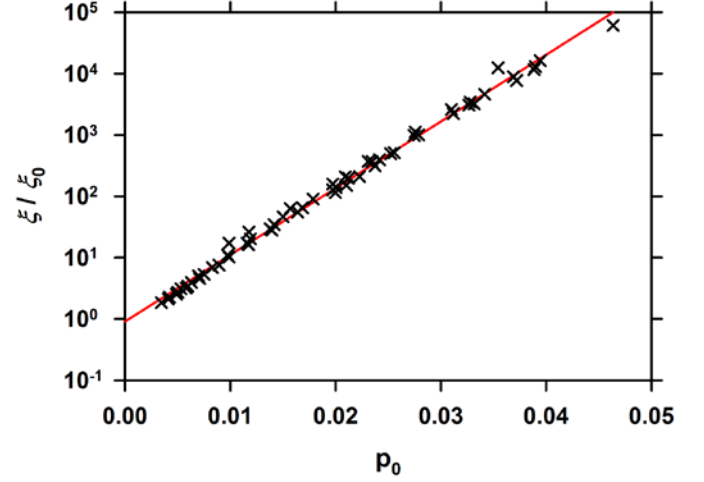


Fig. A2: Amplitude at 20 m for LAMDA simulations in which parameters were varied over ranges given in Table I with $B=0$. The red line is a least squares fit to the data, which yields the constant in Eq. (8).

Table I. Parameter Variations for Scaling Simulations

Parameter		Unit	min	max	nominal
Pipe Radius	b	cm	4	16	5
Conductivity	σ	s^{-1}	3.16E15	6.4E17	1.0E16
Magnetic Field	B	kG	0.3	1.5	0.5
Beam Current	I	kA	0.5	4.0	2.0
Electron Energy	KE	MeV	5	20	10
Pulse Length	τ	μs	0.125	4.0	1.0

B. Continuous Magnetic Guide Field

The parametric scaling of the characteristic growth length in a magnetic guide field is given by (Eq. (4)). Using this as guidance, we define the variable

$$p_B = \frac{I_{kA} \sqrt{\tau_{\mu s}}}{B_{kG} b_{cm}^3 \sqrt{10^{-16} \sigma_{s^{-1}}}} \quad (9)$$

A semi-log plot of the nominal case given in Table I shows that in a magnetic field the instability also grows nearly exponentially with distance, $\xi / \xi_0 \approx \exp(z / \zeta_B)$ (see Fig. A3)

The parameters in Table I were varied, and the growth at 100 m was plotted as a function of p_B (Fig. A4). It is clear that LAMDA simulations closely follow this scaling law for exponential growth of the instability, with an e-folding distance given by

$$\zeta_B = 0.98 \frac{B_{kG} b_{cm}^3 \sqrt{10^{-16} \sigma_s^{-1}}}{I_{kA} \sqrt{\tau_{\mu s}}} \quad (10)$$

The e-folding length ζ_B has the same parametric scaling as z_g in Eq. (4) if $k_0 \approx k_\beta$, which is true for all of the cases simulated.

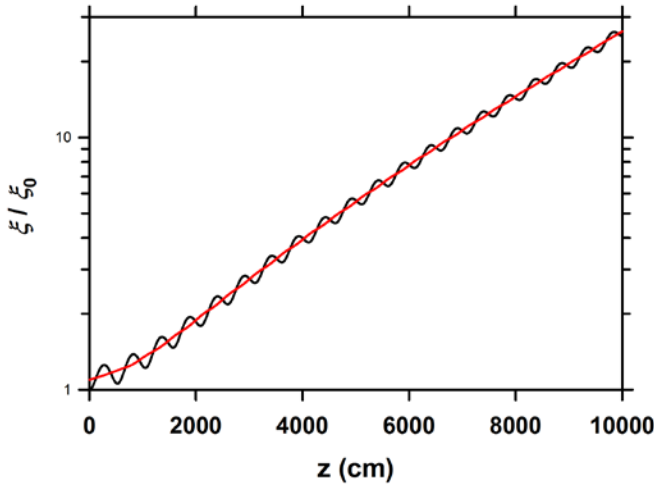


Fig. A3: LAMDA simulation of instability amplitude at the end of a 1- μ s pulse as a function of distance. Parameters for this simulation are those given in the nominal column of Table I. The black curve is the result of the simulation. The red curve has smoothed out the betatron oscillations via localized regression.

As deduced from these LAMDA simulations, the e-folding length ζ_B is about 1.7 times longer than the analytical characteristic length for growth z_g , so using z_g to estimate the effect of this instability in a given accelerator architecture [22] is a very conservative approach.

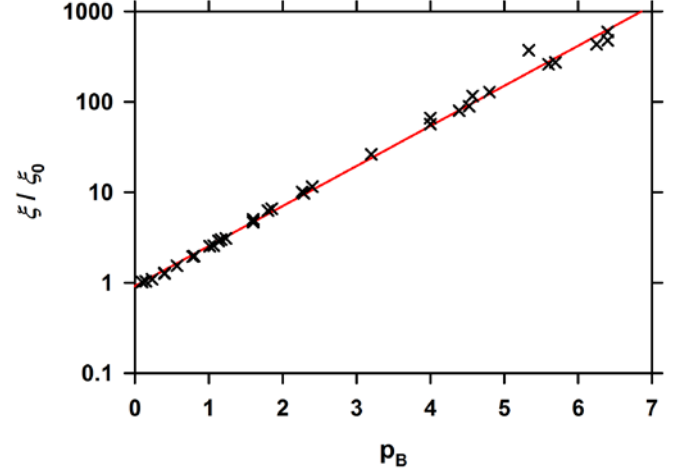


Fig. A4: Instability amplitude at 100 m as a function of parametric variations summarized by the variable $p_B = 10^8 I \sqrt{\tau / \sigma} / B b^3$. Each symbol is the result of a LAMDA simulation with different values of the parameters. The red line is a least square fit to the data, which yields the constant in Eq. (10)..

ACKNOWLEDGMENTS

The author thanks his colleagues at Los Alamos and elsewhere for enlightening discussion about high-power accelerator physics. Special recognition is due C. B. Mostrom and C. Thoma at Voss Scientific and T. H. Hughes at Sandia National Laboratory for their expert advice on the LAMDA beam dynamics code.

REFERENCES

- [1] L. J. Laslett, V. K. Neil and A. M. Sessler, "Transverse resistive instabilities of intense coasting beams in particle accelerators," *Rev. Sci. Instrum.*, vol. 36, no. 4, pp. 436 - 448, 1965.
- [2] S. Bodner, V. K. Neil and L. Smith, "Decay of image currents and some effects on beam stability," *Part. Accel.*, vol. 1, pp. 327 -334, 1970.
- [3] G. J. Caporaso, W. A. Barletta and V. K. Neil, "Transverse resistive wall instability of a relativistic electron beam," *Part. Accel.*, vol. 11, pp. 71 - 79, 1980.
- [4] D. H. Whittum, A. M. Sessler and V. K. Neil, "Transverse resistive wall instability in the two-beam accelerator," *Phys. Rev. A*, vol. 43, no. 1, pp. 294 - 303, 1991.
- [5] R. J. Briggs, D. L. Birks, D. S. Prono, D. Prosnitz and L. L. Reginato, "Induction linac-based FELs," in *Part. Accel. Conf.*, 1987.
- [6] C. J. Lasnier, S. L. Allen, B. Felker and et al., "Burst mode FEL with the ETA-III induction linac," in *Part. Accel. Conf.*, 1993.

- [7] G. Westenskow, G. Caporaso, Y.-J. Chen, T. Houck and S. Sampayan, "Double pulse experiment with a velvet cathode on the ATA injector," in *Part. Accel. Conf.*, 1996.
- [8] S. Chen, X. Li, Z. Huang and et al., "Output of triple-pulse megahertz burst rate high-voltage induction device," *Appl. Phys. Lett.*, vol. 88, pp. 264107-1 - 264107-2, 2006.
- [9] J. J. Deng, J. S. Shi, W. P. Xie and et al., "R&D status of high-current accelerators at IFP," *J. Korean Phys. Soc.*, vol. 59, no. 6, pp. 3619 - 3622, Dec. 2011.
- [10] Y.-J. Chen, L. R. Bertolini, G. J. Caporaso and et al., "Downstream system for the second axis of the DARHT facility," in *LINAC*, Gyeongju, Korea, 2002.
- [11] Y.-J. Chen, L. Bertolini, G. J. Caporaso, D. D.-M. Ho, J. F. McCarrick, A. C. Paul, P. A. Pincosy, B. R. Poole, L.-F. Wang and G. A. Westenskow, "Downstream transport system for the second axis of the Dual-Axis Radiographic Hydrodynamic Test facility," in *14th Int. Conf. High-Power Particle Beams*, Albuquerque, NM, USA, 2002.
- [12] G. V. Stupakov, "Wakefields and instabilities in linacs," in *Int. School on Part. Accel.*, Long Beach, CA, USA, 2002.
- [13] T. P. Hughes, C. B. Mostrom, T. C. Genoni and C. Thoma, "LAMDA user's manual and reference," Voss Scientific Report, VSL-0707, 2007.
- [14] T. Genoni, T. Hughes and C. Thoma, "Improved envelope and centroid equations for high current beams," in *AIP Conf. Proc.*, 2002.
- [15] C. Ekdahl, "Transient decay of beam-produced fields in thin walled tubes," *J. Appl. Phys.*, vol. 89, no. 12, pp. 8214 - 8218, 2001.
- [16] C. Ekdahl and et al., "Suppressing beam motion in a long-pulse linear induction accelerator," *Phys. Rev. ST Accel. Beams*, vol. 14, p. 120401, 2011.
- [17] Y.-J. Chen, "Corkscrew modes in linear induction accelerators," *Nucl. Instrum. Methods Phys. Res.*, vol. A292, pp. 455 - 464, 1990.
- [18] Y.-J. Chen, "Transverse beam instability in a compact dielectric wall induction accelerator," in *Proc. 21st Particle Accel. Conf.*, Knoxville, TN, USA, 2005.
- [19] C. Ekdahl and et al., "Electron beam dynamics in a long-pulse linear induction accelerator," *J. Korean Phys. Soc.*, vol. 59, pp. 3448 - 3452, 2011.
- [20] G. J. Caporaso and Y. -J. Chen, "Electron Induction Linacs," in *Induction Accelerators*, K. Takayama and R. J. Briggs, Eds., New York, Springer, 2011, pp. 117 - 163.
- [21] C. H. Woods, "The image instability in high current linear accelerators," *Rev. Sci. Instrum.*, vol. 41, no. 7, pp. 959 - 962, 1970.
- [22] C. Ekdahl, "Electron-beam dynamics for an advanced flash-radiography accelerator," *IEEE Trans. Plasma Sci.*, vol. 43, no. 12, pp. 4123 - 4129, Dec. 2015.
- [23] M. J. Burns, B. E. Carlsten, T. J. T. Kwan and et al, "DARHT accelerators update and plans for initial operation," in *Part. Accel. Conf.*, New York, 1999.
- [24] C. Ekdahl, "Modern electron accelerators for radiography," *IEEE Trans. Plasma Sci.*, vol. 30, no. 1, pp. 254-261, 2002.
- [25] K. Peach and C. Ekdahl, "Particle radiography," *Rev. Acc. Sci. Tech.*, vol. 6, pp. 117 - 142, 2013.
- [26] Y.-J. Chen and A. C. Paul, "Physics design considerations of Diagnostic X beam transport system," in *20th Int. Linac Conf.*, Monterey, CA, USA, 2000.